Aerodynamic and Aeroacoustic Performance of a Propeller Propulsion System with Swirl-Recovery Vanes

Sinnige, Tomas; Stokkermans, Tom; Ragni, Daniele; Eitelberg, Georg; Veldhuis, Leo

DOI
10.2514/1.B36877

Publication date
2018

Document Version
Final published version

Published in
Journal of Propulsion and Power: devoted to aerospace propulsion and power

Citation (APA)
Sinnige, T., Stokkermans, T., Ragni, D., Eitelberg, G., & Veldhuis, L. (2018). Aerodynamic and Aeroacoustic Performance of a Propeller Propulsion System with Swirl-Recovery Vanes. *Journal of Propulsion and Power: devoted to aerospace propulsion and power*, *34*(6), 1376-1390. https://doi.org/10.2514/1.B36877

JOURNAL OF PROPULSION AND POWER
Vol. 34, No. 6, November–December 2018

Aerodynamic and Aeroacoustic Performance of a Propeller Propulsion System with Swirl-Recovery Vanes

Tomas Sinnige,* Tom C. A. Stokkermans,† Daniele Ragni,‡ Georg Eitelberg,§
and Leo L. M. Veldhuis§
Delft University of Technology, 2629 HS Delft, The Netherlands

DOI: 10.2514/1.B36877

Swirl-recovery vanes (SRVs) enhance propulsive efficiency by converting the rotational kinetic energy in a propeller slipstream into additional thrust. This paper discusses the aerodynamic and aeroacoustic impact of the installation of a set of SRVs downstream of a single-rotating propeller. Experiments were carried out in a large low-speed wind tunnel, whereas simulations were performed by solving the Reynolds-averaged Navier–Stokes equations. Favorable comparisons between the experimental and numerical slipstream data validated the simulations, which predicted a maximum propulsive-efficiency increase of 0.7% with the current design of the SRVs. This can be improved further by optimizing the pitch distribution of the SRVs. The upstream effect of the SRVs on the time-averaged propeller performance was negligible. Yet, small but systematic unsteady propeller loads were measured with a peak-to-peak amplitude of at most 2% of the time-averaged loading, occurring at a frequency corresponding to the five SRV passages during one revolution. The downstream interaction was one order of magnitude stronger, with unsteady loading on the SRVs with a peak-to-peak amplitude of about 20% of the time-averaged load. The interaction mechanisms caused an increase of the tonal noise levels of 3–7 dB, with the noise penalty decreasing with increasing propeller thrust setting.

Nomenclature

B	=	number of propeller blades
BPF	=	blade-passage frequency, nB, Hz
C_p	=	pressure coefficient, $(p - p_\infty)/q_\infty$
C_Q	=	propeller torque coefficient, $Q/\rho_\infty n^2 D^5$
C_T	=	propeller thrust coefficient, $T/\rho_\infty n^2 D^4$
$C_{T_{\mathrm{SRV}}}$	=	swirl-recovery-vane thrust coefficient, $T_{\mathrm{SRV}}/\rho_\infty n^2 D^4$
c	=	propeller-blade chord, m
c'_n	=	unsteady propeller-blade normal-force coefficient, $n'/q_\infty c$
$c'_{n_{\mathrm{SRV}}}$	=	unsteady swirl-recovery-vane normal-force coefficient, $n'_{\mathrm{SRV}}/q_\infty c_{\mathrm{SRV}}$
c_{SRV}	=	swirl-recovery-vane chord, m
$c_{t_{\mathrm{SRV}}}$	=	sectional swirl-recovery-vane thrust coefficient, $t_{\mathrm{SRV}}/\rho_\infty n^2 D^3$
D	=	propeller diameter, m
F_{SRV}	=	resultant force on swirl-recovery vane, N
f	=	frequency, Hz
h_i	=	grid cell size of grid i
J	=	advance ratio, V_∞/nD
k	=	turbulence kinetic energy, $\mathrm{m}^2/\mathrm{s}^2$
n	=	propeller rotational speed, Hz
n'	=	unsteady sectional propeller-blade normal force, N/m
n_{BPF}	=	number of tones (blade-passage-frequency multiples) used to compute cumulative tonal noise level
n'_{SRV}	=	unsteady sectional swirl-recovery-vane normal force, N/m
p	=	static pressure, Pa; acoustic pressure, Pa; order of convergence
$p_{i\cdot\mathrm{BPF}}$	=	acoustic pressure associated with the tone at the ith multiple of the blade-passage frequency, Pa
p_∞	=	freestream static pressure, Pa
Q	=	propeller torque, N · m
q_∞	=	freestream dynamic pressure; $\rho_\infty V_\infty^2/2$, Pa
R	=	propeller radius, m
R_{hub}	=	propeller-hub radius, m
R_{nac}	=	nacelle radius, m
R_{SRV}	=	swirl-recovery-vane radius, m
r	=	radial coordinate, m
r_{mic}	=	distance from propeller center to microphone, m
T	=	propeller thrust, N
T_{SRV}	=	swirl-recovery-vane thrust, N
T_∞	=	freestream static temperature, K
t_{SRV}	=	sectional swirl-recovery-vane thrust, N/m
U_{s}	=	standard deviation of fit based on apparent order of convergence
U^*_{s}	=	standard deviation of fit based on theoretical order of convergence
U_ϕ	=	estimated discretization uncertainty based on apparent order of convergence
U^*_ϕ	=	estimated discretization uncertainty based on theoretical order of convergence
V	=	velocity magnitude, m/s
V_{a}	=	axial velocity, m/s
V_{t}	=	tangential velocity, m/s
V_∞	=	freestream velocity, m/s
X	=	axial coordinate, m
x	=	chordwise coordinate, m
Y	=	lateral coordinate, m
y^+	=	nondimensional wall distance
Z	=	vertical coordinate, m
α	=	angle of attack, deg
β	=	angle of sideslip, deg
β_{SRV}	=	swirl-recovery-vane pitch angle, deg
$\Delta\dot{E}_{k_{\mathrm{rot}}}$	=	change in rotational kinetic-energy flow due to the propulsion system, J/s
$\Delta\dot{E}_{k_{\mathrm{tot}}}$	=	change in total kinetic-energy flow due to the propulsion system, J/s
$\Delta\eta$	=	change in propulsive efficiency due to installation of the swirl-recovery vanes, $\eta_{\mathrm{SRVs\text{-}on}} - \eta_{\mathrm{SRVs\text{-}off}}$

Presented as Paper 2015-2358 at the 21st AIAA/CEAS Aeroacoustics Conference, Dallas, TX, 22–26 June 2015; received 17 August 2017; revision received 13 March 2018; accepted for publication 16 May 2018; published online 27 August 2018.

*Ph.D. Candidate, Flight Performance and Propulsion Section, Faculty of Aerospace Engineering, Kluyverweg 1; T.Sinnige@tudelft.nl. Member AIAA.

†Ph.D. Candidate, Flight Performance and Propulsion Section, Faculty of Aerospace Engineering, Kluyverweg 1; T.C.A.Stokkermans@tudelft.nl. Member AIAA.

‡Assistant Professor, Aeroacoustics Section, Faculty of Aerospace Engineering, Kluyverweg 1; D.Ragni@tudelft.nl. Member AIAA.

§Full Professor, Flight Performance and Propulsion Section, Faculty of Aerospace Engineering, Kluyverweg 1. Member AIAA.

ϵ_V = uncertainty of instantaneous velocity magnitude from particle-image velocimetry, m/s
$\eta_{\text{SRVs-off}}$ = propulsive efficiency without swirl-recovery vanes installed
$\eta_{\text{SRVs-on}}$ = propulsive efficiency with swirl-recovery vanes installed
θ = geometric axial directivity angle, deg
θ_e = axial emission angle, deg
ρ_∞ = freestream air density, kg/m^3
ΣSPL = cumulative tonal noise level, dB [Eq. (1)]
ϕ = circumferential blade position, deg; circumferential directivity angle, deg
ϕ_i = numerical solution obtained using grid i
$\phi_{\text{LE}}^{r/R\approx 0.65}$ = circumferential position of blade leading edge at $r/R \approx 0.65$, deg
ϕ_{SRV} = circumferential position of swirl-recovery vane, deg
ϕ_0 = estimated exact numerical solution
ω = specific turbulence dissipation rate, 1/s
ω_X = vorticity in axial direction, 1/s

I. Introduction

PROPELLER propulsion systems have the potential to enable a step change in terms of fuel consumption and emissions of future passenger aircraft. Compared to turbofan engines, the higher mass-flow rates and lower exhaust velocities characteristic of propellers result in an increased propulsive efficiency. In a recent design study [1], the corresponding fuel-burn reduction was estimated at approximately 10–20% when compared to an equivalent-technology-level geared turbofan. Besides increasing the axial momentum in the propeller slipstream, a single-rotating propeller also adds a swirl component to the downstream flow. Because this swirl component does not add to the thrust, its generation can be considered as a loss mechanism.

To further increase the propulsive efficiency of single-rotating propellers, the rotational kinetic energy in the propeller slipstream should be converted into additional thrust. This can be achieved by installing a second blade row, rotating in the opposite direction of the front rotor. Such a configuration is commonly referred to as contrarotating open rotor and has been studied extensively in the literature [2–4]. Alternatively, stationary swirl-recovery vanes (SRVs) can be used, functioning similarly to stator vanes employed in turbomachinery. Like contrarotating open rotors, SRVs use the swirl in the propeller slipstream to generate thrust, thereby enhancing the propulsive performance. However, installation of the SRVs adds less complexity to the propulsion system when compared to the contrarotating solution.

In order for the SRVs to increase the propulsive efficiency of the already highly efficient single-rotating propeller, their integration with the propulsion system is critical. Previous research by NASA confirmed the potential of SRVs to enhance the propulsive efficiency, with measured efficiency gains of about 2% in cruise conditions [5]. Numerical analyses using an Euler solver, on the other hand, predicted a propulsive-efficiency increase of approximately 5% for the same configuration and operating conditions [6]. This indicates that the viscous drag needs to be taken into account during both analysis and design of the SRVs. A more recent computational-fluid-dynamics (CFD) analysis using a Reynolds-averaged Navier–Stokes (RANS) solver showed increased thrust levels due to application of SRVs [7]. However, in the same study, it was found that the total system efficiency was reduced, stressing the importance of proper SRV design and integration. This was addressed by a follow-up work of the same research group [8], focusing on the development, application, and experimental validation of a low-fidelity tool for SRV design. In this work, a measured 2.6% increase in thrust was reported at the design condition for high propeller thrust at low flight velocity and low Reynolds number. Additional design studies [9] highlighted the sensitivity of SRV performance to the selection of the vane count, the design point, and airframe installation effects. Detailed flowfield information of the propeller–SRV configuration has not been published in literature though, and the existing numerical studies do not contain thorough validations with experimental data.

Apart from the modification of the time-averaged propulsive performance, the installation of the SRVs introduces two unsteady interactions. First, the propeller blade loading becomes unsteady due to the periodic disturbance experienced by the propeller blades when passing by in front of the SRVs. Second, the SRV loading is unsteady due to the periodic fluctuations induced on the SRVs by the propeller-blade wakes and tip vortices. Both effects have been confirmed by transient simulations using a profile-transformation method, hence simulating a single blade passage only [10]. The aerodynamic interaction mechanisms for the propeller–SRV configuration are largely similar to rotor–stator interactions occurring in turbomachinery, as discussed in, for example, Refs. [11,12]. However, for the propeller–SRV configuration, the reduced frequency is lower and the axial spacing between the rotating and stationary rows is larger than for conventional turbomachinery configurations.

The unsteady loading on the propeller and SRVs causes two additional noise sources. However, the only acoustic measurements published thus far for a configuration with SRVs installed showed a small noise reduction in the cruise condition when compared to the isolated propeller configuration [13]. This was attributed to the observed unloading of the propeller, which decreased the steady-loading noise. Apparently, in this case the reduction in steady-loading noise was sufficient to offset the interaction noise caused by the unsteady loading on the propeller blades and the SRVs.

The existing evaluations of the performance of SRVs have only focused on integrated aerodynamic parameters, such as thrust and torque. Moreover, the aeroacoustic impact of SRVs has only been assessed for high-speed cases, with relatively little detail. As such, a detailed understanding of the effect of SRVs on the flowfield, the resulting unsteady interactions, and the aeroacoustic behavior is still missing. Such understanding is of crucial importance for the successful design of SRVs, which are to deliver the maximum performance benefit compared to an isolated single-rotating propeller. The study discussed in the current paper aimed at filling these knowledge gaps by providing a detailed analysis of the propeller-slipstream flowfield, the steady and unsteady propulsive performance, and the noise emissions of the system with and without SRVs installed. A joint experimental–numerical approach was taken, in which the simulations were validated using the experimental data and then analyzed to obtain additional information, which could not be measured in the experiment.

II. Methods

A. Experimental Setup

1. Wind-Tunnel Facility

The experiments were performed at the large low-speed facility of the German–Dutch wind tunnels (DNW–LLF). This closed-circuit low-speed wind tunnel was operated in the open-jet configuration, with an 8×6 m outlet. At the selected freestream velocity (60 m/s), the turbulence intensity is 0.24% in the longitudinal direction and 0.13% in the lateral direction. The test hall is treated with acoustic liners to achieve a semi-anechoic environment.

2. Models

A combination of a propeller and downstream SRVs was mounted on a support structure in the wind tunnel, as shown in Fig. 1. Figure 2 provides a technical drawing of the models, including the definition of the Cartesian and polar coordinate systems used throughout the paper. The origin of both coordinate systems is defined at the intersection of the propeller axis and the pitch change axis of the blades.

The propeller featured a diameter of 0.508 m and six highly swept blades, representative of a high-speed propeller design. The model was developed and used before in the Advanced Propulsion Integration Aerodynamics and Noise (APIAN) project [14] funded by the European Union. The blade pitch angle at $r/R = 0.75$ was set to 40.4 deg with respect to the local chord line, with the pitch angle defined such that the blade section is aligned with the rotational direction for a pitch angle of 0 deg.

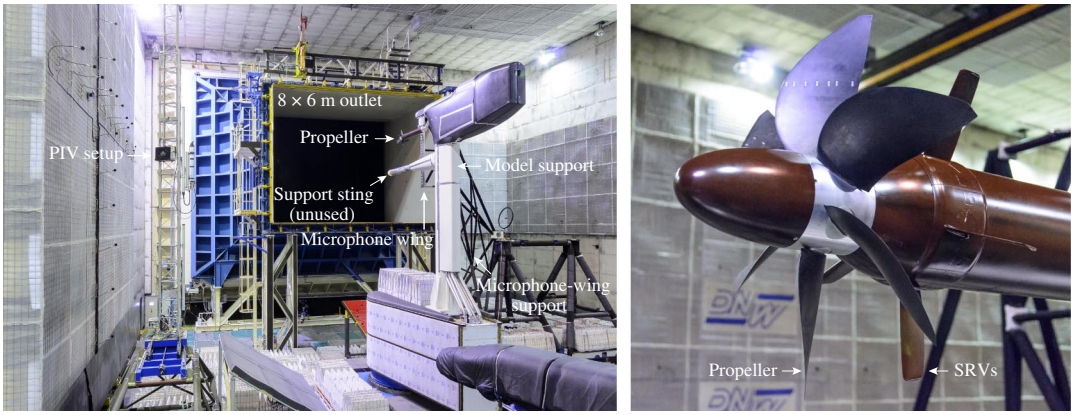

a) Overview of test setup b) Propeller–SRV configuration

Fig. 1 Test setup installed in the wind tunnel.

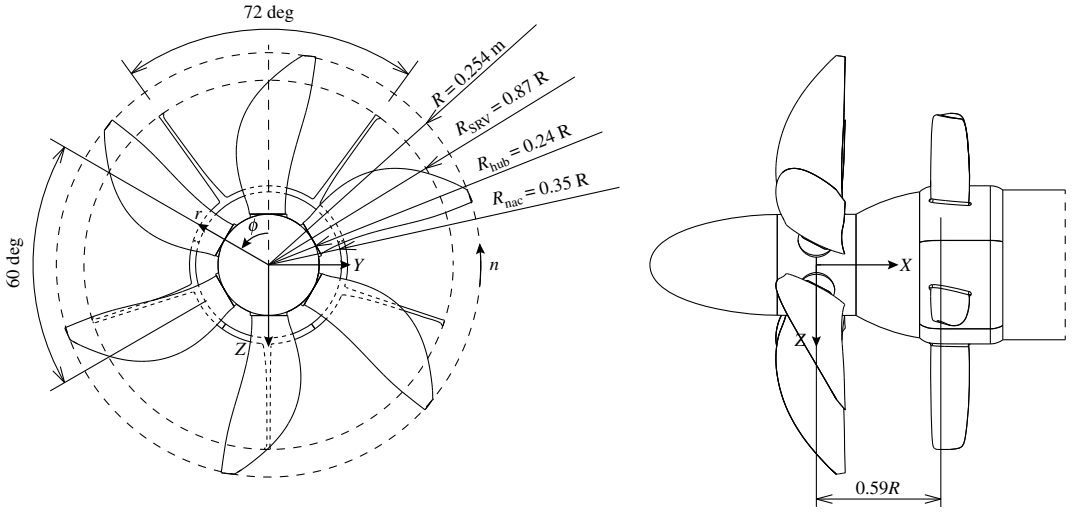

a) Front view b) Side view

Fig. 2 Technical drawing of the propeller–SRV configuration.

The SRVs were designed to achieve a positive efficiency increase for advance ratios up to $J = 1.75$. Although not optimized for maximum aerodynamic or aeroacoustic performance, the used SRV geometry introduced all flow phenomena relevant to a typical propeller–SRV configuration. Therefore, it is considered adequate for the purpose of this paper. The radial distributions of the chord and pitch of the SRV satisfying the design objective were defined using an in-house-developed low-fidelity design method based on the propeller analysis and design program XROTOR [15]. In this process, the number of SRVs, the SRV radius, and the propeller–SRV spacing were fixed. A total of five vanes was chosen to limit the interaction noise by reducing the number of both total and concurrent interactions compared to an axisymmetric propeller–SRV configuration with six SRVs. The SRVs were distributed around the nacelle at circumferential angles of $\phi_{SRV} = [36, 108, 180, 252, 324]$ deg. To minimize additional noise due to the interaction between the tip vortices of the propeller blades and the SRVs, the radius of the SRVs was set to 90% of the local contracted slipstream radius, resulting in an SRV radius of 87% of that of the propeller. The spacing between the propeller and the SRVs was equal to approximately 60% of the propeller radius. The selected distributions of the SRV chord and pitch angle are shown in Fig. 3. The pitch angle β_{SRV} is defined here in the same way as used for the propeller blade. A symmetrical airfoil was selected for the entire vane; manufacturing constraints on the minimum thickness led to the selection of a NACA 0009 profile. Later studies [8,9], performed after the work discussed in the current paper had been completed, showed that cambered airfoils typically provide better performance.

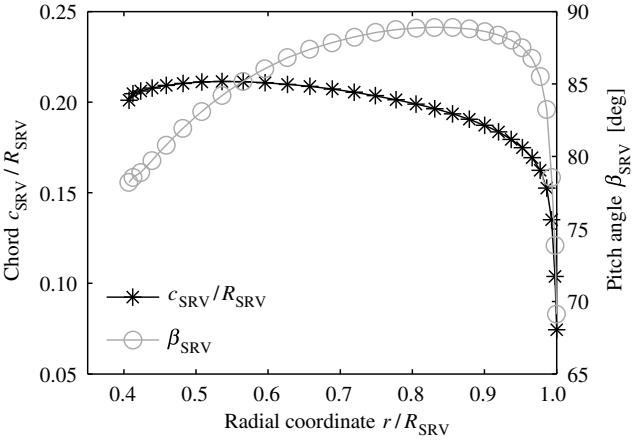

Fig. 3 Radial distributions of the chord and pitch angle of the SRVs.

3. *Measurement Techniques*

The propeller was connected to a rotating shaft balance (RSB), which provided measurements of the propeller thrust and torque during operation. Because the RSB was connected to the entire rotating part of the setup, the forces acting on the spinner and propeller hub were also included. The thrust data were corrected for the pressure acting on the back of the propeller hub by measuring the static pressure in the small gap between the propeller hub and the

front of the motor. The resulting force was subtracted from the raw RSB data to obtain the corrected propeller thrust.

Miniature surface-pressure transducers were integrated into the propeller blades to obtain phase-accurate pressure distributions. At a radial station of $r/R \approx 0.65$, seven sensors were installed on both the suction and pressure sides of the blades, providing pressure data at chordwise locations of $x/c = [0.05, 0.15, 0.30, 0.45, 0.60, 0.70, 0.90]$ on the suction side and $x/c = [0.05, 0.15, 0.30, 0.45, 0.60, 0.75, 0.90]$ on the pressure side. The transducers measured pressure fluctuations in the frequency range of 0–10 kHz. The raw measurement data were postprocessed by phase locking with a one-per-revolution trigger signal. Subsequently, the measured pressure jump between the pressure and suction sides of the blade was integrated using the trapezoidal rule to obtain the local normal force (thus neglecting the contribution of the viscous forces). To account for the steep pressure gradient near the airfoil's leading edge, the pressure jump measured at the pressure transducer closest to the blade leading edge ($x/c = 0.05$) was prescribed up to the leading edge. Moreover, at the trailing edge, a pressure difference of zero was prescribed. The validity of this approach was assessed by a comparison with downsampled CFD data for the isolated propeller, which showed that the associated integration error was less than 1%.

The SRVs were not instrumented, so no vane-loading information was available from the experiment. The effects of the SRVs on the flowfield in the propeller slipstream were quantified using stereoscopic particle-image velocimetry (PIV). The measurements were taken in longitudinally adjacent planes, located slightly below the propeller axis at a vertical position of $Z/R = 0.03$ due to a small misalignment of the setup. The position of the evaluation plane with respect to the models is illustrated in Fig. 4. Table 1 provides a detailed description of the data-acquisition and postprocessing characteristics of the PIV setup. All image pairs were acquired phase locked to the propeller-blade phase angle, providing flowfield data for 11 equally spaced circumferential blade positions with 50 images per phase angle. The time-averaged flowfields were approximated by averaging the results obtained at the individual phase angles. The data extracted from the separate planes were combined after postprocessing to obtain a single representation of the propeller-slipstream flow. The uncertainty of the velocity measurements was estimated from the correlation statistics, following the method by Wieneke [16]. The computed uncertainty on the instantaneous velocity fields was averaged over all available images, resulting in an uncertainty on the velocity magnitude ϵ_V of approximately 2.5% of the freestream velocity.

The aeroacoustic impact of the installation of the SRVs was quantified using microphones integrated into a wing-shaped structure that was positioned in the flow at a sideline distance of 2.8 m from the propeller center. A technical drawing of the aeroacoustic measurement setup is depicted in Fig. 5. The microphone wing was equipped with 1/4 in. pressure-field microphones, featuring a flat response (±1 dB) in the frequency range of 4–25,000 Hz, an electronic noise level below 40 dB, and a maximum input level of 168 dB. The microphones were installed recessed in the microphone wing, in individual cavities covered by wire meshes. By traversing the microphone wing through the test hall in the axial direction, a geometric axial directivity range was covered of $30 \leq \theta \leq 150$ deg. The corresponding circumferential directivity angles equaled $57 \leq \phi \leq 111$ deg. The definition of both directivity angles is included in Fig. 5. The data presented in this paper were obtained

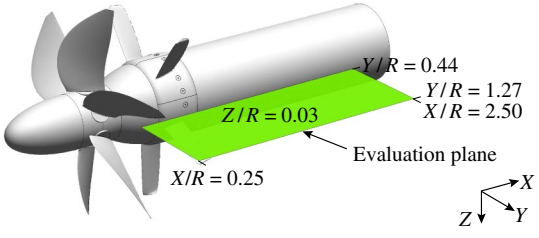

Fig. 4 Position of the evaluation plane used in the PIV measurements.

Table 1 PIV setup and data-acquisition characteristics

Parameter	Value
Laser	Nd:YAG 200 mJ
Cameras	2 × 1.3 Mpixel (CCD sensor)
Pixel size	6.7 × 6.7 μm
Objective	200 mm $f/2.0$ + 2× teleconverter
Field-of-view (FOV) dimensions	572 × 212 mm
Vertical position FOV (Z/R)	0.03
Final interrogation window size	24 × 24 pixel
Window overlap factor	50%
Magnification	0.040
Digital resolution	6.0 pixel/mm
Pulse separation	15 μs
Freestream shift	5–7 pixel
Number of image pairs	550
Acquisition frequency	3.0 Hz
Vector spacing	2.0 mm
Uncertainty ϵ_V/V_∞	0.025

CCD = charge-coupled device.

using the microphone at $\phi = 90$ deg, positioned at a distance of $r_{\text{mic}} = 2.8$ m from the propeller center at $\theta = 90$ deg. All microphone acquisitions were performed for 30 s at a sampling rate of 51.2 kHz. The acoustic spectra were computed using Welch's method [17] with 94 blocks, no overlap, and Hann windows, resulting in a frequency resolution of around 3 Hz. The tonal noise levels were extracted from the raw measurement data using the same phase-locking technique as applied to the surface-pressure data.

B. Numerical Setup

1. *Numerical Scheme*

The numerical study was performed by solving the compressible RANS equations using ANSYS® CFX release 16.0, an unstructured, element-based node-centered finite-volume solver [18]. To capture the unsteady aerodynamic interaction between the propeller and the SRVs, the governing equations were solved in a time-dependent manner by a second-order backward Euler scheme. A time step equivalent to 1 deg of propeller rotation was used, as commonly found in the literature [19,20]. The simulations were performed for 840 deg of propeller rotation, of which only the last 120 deg were used to eliminate startup effects. Discretization of the advection term was done with an upwind scheme using the Barth–Jespersen boundedness principle [21] to be close to second-order accurate. The spatial derivatives of all diffusion terms were evaluated using shape functions following the standard finite-element approach. The alternate rotation model was used. A fully turbulent flow was prescribed using the $k-\omega$ turbulence model with shear-stress-transport correction. An automatic near-wall treatment was applied, switching between solving the viscous sublayer and using scalable wall functions. For the lowest advance ratio, the most critical case in terms of the blade loading, y^+ was 11 on average and 30 at maximum, resulting in the use of wall functions.

2. *Computational Domain and Boundary Conditions*

The computational domain is illustrated in Fig. 6. For the isolated propeller simulations, only a single blade was simulated in a 60 deg wedge-shaped domain with cyclic periodic boundary conditions. The inlet and far field were placed at a distance of $5R$ from the propeller, similar to the approach taken by Ortun et al. [20] for the same propeller, whereas the outlet was placed further away at $10R$ to reduce disturbances in the static-pressure field. The simulation data were analyzed to verify that the domain was sufficiently large. In terms of boundary conditions, the total pressure was prescribed on the inlet. On the outlet, the spatial average of the static pressure was specified to equal the freestream static pressure. Finally, the far field was modeled with a slip-wall boundary condition. The inlet conditions matched the experimental conditions listed in Table 2, except for the turbulence quantities. Instead, the inlet turbulence was

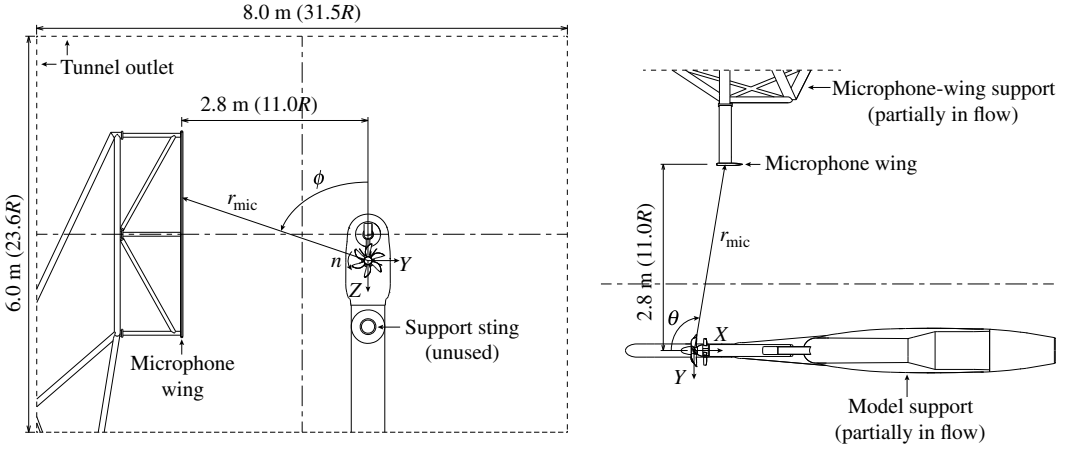

Fig. 5 Technical drawing of the aeroacoustic measurement setup.

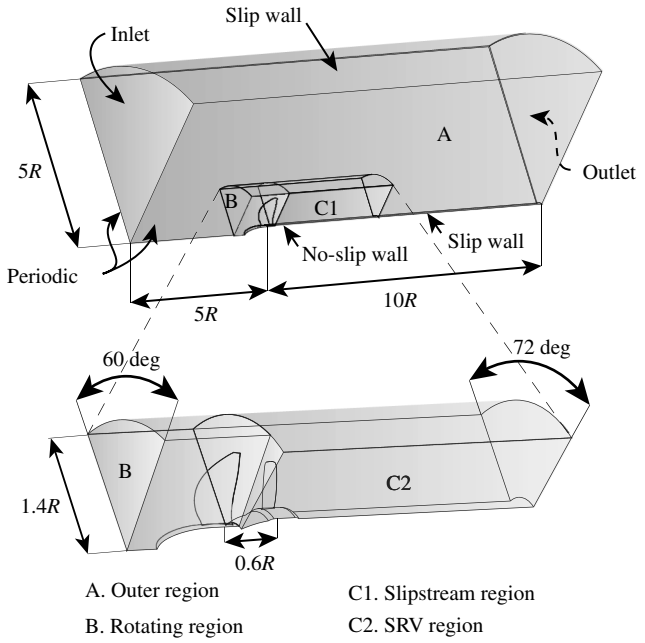

Fig. 6 Definition of the computational domain; full annulus was simulated with SRVs installed.

set based on the recommendations of Spalart and Rumsey [22], resulting in $k = 0.0036\ \text{m}^2 \cdot \text{s}^{-2}$ and $\omega = 1127\ \text{s}^{-1}$. The ideal-gas law was applied as equation of state, whereas the dynamic viscosity was obtained with Sutherland's law using standard atmospheric conditions. For the propeller–SRV simulations, periodicity is not applicable, hence the full annulus was simulated. An exception was made to reduce the computational cost for the grid-convergence study of the SRVs, for which a profile transformation was applied to couple the rotating region (B in Fig. 6) and the SRV region (C2 in Fig. 6). In this way, the unequal pitch of the propeller and SRV domains was mitigated by a scaling of the flow profile across the interface between the propeller and the SRVs. This allowed for a simulation of a single blade and SRV to be made [18], which significantly reduced the computational cost of the unsteady simulations performed for the grid-convergence study.

The grid was created with ANSYS Meshing release 16.0, and featured a triangular wall grid, 12 layers of semistructured prismatic elements adjacent to all no-slip walls, and tetrahedral elements in the rest of the computational domain. On the periodic boundaries, the grid was conformal to avoid interpolation. For the full annulus, the grid was copied and rotated to achieve periodicity in the grid. An additional grid refinement was applied to the slipstream and SRV regions to avoid numerical diffusion of the propeller slipstream as much as possible. Also, the propeller surface grid required an additional refinement to capture the effect of a leading-edge vortex on the blade loading.

3. *Grid-Convergence Study and Error Estimation*

Grid-convergence studies were performed for the isolated propeller and for the propeller–SRV configuration. Two sets of five grids were generated, with grid sizes as reported in Table 3. Refinement and coarsening were applied to the local cell sizes with a ratio of 1.3, except for the inflation layer. This layer was kept constant for constant y^+, following Roache [23].

Figure 7a displays the effect of grid refinement on the pressure distribution on the front part of the blade's suction side at $r/R \approx 0.65$. The isolated propeller is considered at a high loading condition ($J = 1.05$). The effect of grid refinement is small and only noticeable in an area of reduced pressure just aft of the suction peak. This is the result of a leading-edge vortex occurring at this advance ratio, as discussed in more detail in Sec. III.B.1. This vortex and its pressure gradient are captured better with grid refinement [24], resulting in small changes in thrust and torque coefficient of the propeller blade. To assess the effect of grid refinement on the flowfield in the propeller slipstream, the time-averaged radial distribution of tangential velocity in a plane at $X/R = 1.5$ is shown in Fig. 7b. Differences between the solutions obtained using the different grids are only noticeable in the regions of the tip vortex and the root vortex, whereas outside of these regions the velocity profile remained practically unchanged. The sensitivity of the vortical-flow

Table 2 Flow conditions of the various test cases

J	SRVs	V_∞, m/s	p_∞, hPa	T_∞, K
1.05	Off	60.1	1010.0	299.0
	On	60.1	1019.6	299.3
1.40	Off	60.1	1010.2	298.8
	On	60.0	1019.5	299.0
1.75	Off	60.1	1010.3	298.0
	On	60.0	1019.2	299.0

Table 3 Grid sizes of wedge-shaped domain with SRVs off and on

	SRVs off		SRVs on	
Grid number	Number of nodes	h_i/h_1	Number of nodes	h_i/h_1
5	1,509,555	2.41	2,367,946	1.74
4	2,219,976	1.97	3,356,779	1.55
3	3,406,920	1.58	4,966,426	1.36
2	5,461,761	1.27	7,630,369	1.18
1	9,084,698	1.00	12,188,588	1.00

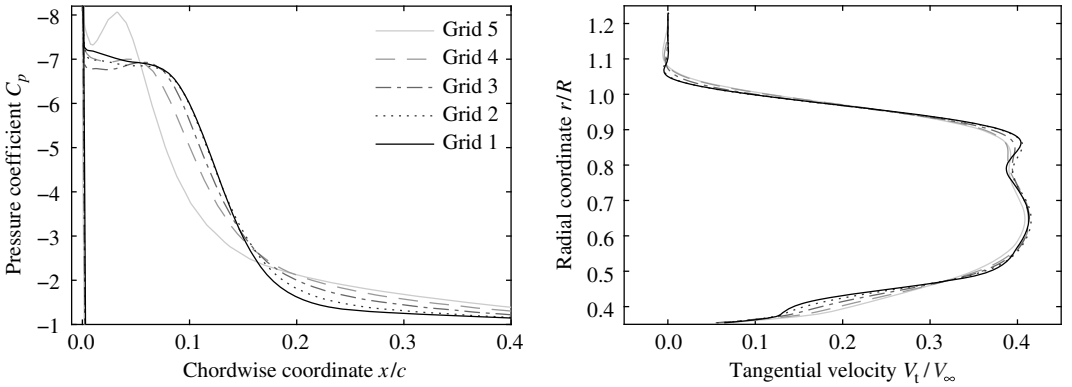

a) Blade pressure distribution at $r/R \approx 0.65$, close-up **b) Tangential-velocity distribution at $X/R = 1.5$**

Fig. 7 Effect of grid refinement for the isolated propeller at $J = 1.05$.

structures to the grid size is a well-known characteristic of second-order schemes, and is caused by numerical diffusion in the solution algorithm [25].

To quantify the discretization uncertainty U_ϕ, the least-squares fitting methodology of Eça and Hoekstra [26] was used. The grid dependency of the propeller thrust coefficient, propeller torque coefficient, and resultant force on the SRVs is summarized in Table 4. The study for the isolated propeller was performed at $J = 1.05$, because this is the most stringent operating condition in terms of loading of the propeller blades. For this case, monotonic convergence was observed. Minor changes in thrust coefficient and torque coefficient occurred due to grid refinement, as illustrated in Figs. 8a and 8b. The apparent order of convergence was higher than the theoretical order of the scheme, resulting in the use of the theoretical order ($p = 2$) to estimate the error. Also, for the theoretical order, a good fit was found (Figs. 8a and 8b). For grid 3, the estimated discretization errors for the thrust coefficient and torque coefficient are 2.44 and 1.97%, respectively.

The study for the configuration with SRVs installed was carried out at $J = 1.75$. At this setting, the propeller loading was least sensitive to the grid size; hence, the effects of refinements near the SRVs could be studied best. For this case, oscillatory convergence occurred for the propeller thrust and torque. Therefore, a conservative error estimate was obtained by taking the maximum difference between the solutions obtained at all grids times an increased safety factor of 3 [26]. This resulted in discretization errors of 1.26 and 1.91% for the thrust coefficient and the torque coefficient, respectively. The resultant force on the vane R_{SRV} converged with some noise (Fig. 8c). Again, the order of convergence was overpredicted by the best fit, and a fit with the theoretical order was used to estimate a discretization error of 2.55% for grid 3.

Combining the results for the isolated propeller and the propeller–SRV configuration, it is concluded that grid 3 provides a sufficiently converged solution to use for the remainder of this study. Therefore, all results presented in the following were obtained with grid 3.

C. Test Cases

All evaluations presented in this paper are based on a freestream velocity of $V_\infty = 60$ m/s, which is the default setting for acoustic measurements at the DNW–LLF. Symmetric inflow conditions were considered ($\alpha = \beta = 0$ deg), whereas three different propeller operating conditions were evaluated, corresponding to high-, medium-, and low-thrust conditions. The associated advance ratios were $J = 1.05$, 1.40, and 1.75, leading to measured propeller thrust coefficients of $C_T = 0.51$, 0.36, and 0.18, respectively. The advance ratio will be used in this paper to refer to the specific thrust settings. For the range of thrust conditions considered, the Reynolds number at a blade section of the propeller at $r/R \approx 0.65$ was approximately 600,000–900,000. At the same radial coordinate, the Reynolds number of the SRVs was around 200,000–300,000. Previous measurements [27] have shown that at the high-thrust condition ($J = 1.05$), the propeller operated right at the onset of nonlinearities in the thrust response. All measurements were taken with and without the SRVs installed. The exact flow conditions of each case can be found in Table 2.

Table 4 Grid dependency of propeller and SRV performance

	$J = 1.05$, SRVs off		$J = 1.75$, SRVs on		
	C_T	C_Q	C_T	C_Q	F_{SRV}
p	2.42	3.81	— —	— —	6.35
U_s, %	0.21	0.20	— —	— —	0.36
U_s^*, %	0.23	0.31	— —	— —	0.56
ϕ_0	0.523	0.157	— —	— —	5.946 N
U_{ϕ_s}, %	2.44	1.97	1.26	1.91	2.55

III. Results

A. Slipstream Flowfield

The installation of the SRVs downstream of the propeller modifies the slipstream flowfield. The PIV setup was used to measure the velocity fields for the cases with and without SRVs. These results were compared to the CFD data to validate the simulations, which were in turn analyzed for a more detailed quantification of the swirl recovery achieved by the SRVs.

1. *Velocity Fields*

The goal of the SRVs is to convert the angular momentum of the swirl in the propeller slipstream into a force in the thrust direction. To compare the distribution of the swirl in the slipstream with and without SRVs installed, Fig. 9 presents contours of the measured and computed nondimensionalized tangential velocity at the position of the PIV measurement plane. The intermediate-thrust condition ($J = 1.40$) is considered, because at this propeller setting the SRVs delivered the largest efficiency increase (see Sec. III.B.2). The experimental results were acquired phase locked to the propeller-blade position; the CFD data were extracted such that they correspond to the same circumferential position of the blade. No experimental data were available around $X/R = 0.6$ for the configuration with SRVs due to reflections from the nearby SRVs. It should be noted that with the SRVs installed, the setup is no longer axisymmetric; hence, the single evaluation plane considered in Fig. 9 is not necessarily representative of the velocity distribution in the entire slipstream.

The contours of the tangential velocity plotted in Fig. 9 indicate that the SRVs reduced the swirl in the propeller slipstream. Downstream of the SRVs ($X/R \geq 0.6$), the tangential velocity component was decreased over the radial extent of the slipstream covered by the SRVs ($Y/R < 0.9$) when compared to the result obtained for the isolated propeller. Because of the cropping of the SRVs relative to the propeller diameter, the swirl in the outboard region of the slipstream ($Y/R \geq 0.9$) could not be recovered. In fact, the swirl velocity was enhanced in this region due to the loading on the SRVs. Upstream of

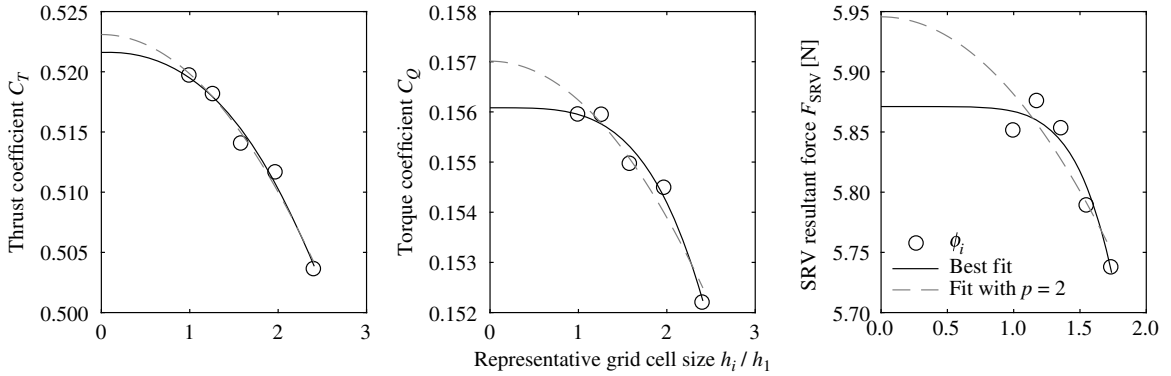

a) Propeller thrust ($J = 1.05$, SRVs off) **b) Propeller torque ($J = 1.05$, SRVs off)** **c) SRV resultant force ($J = 1.75$)**

Fig. 8 Grid convergence for a–b) the isolated propeller and c) the propeller with SRVs.

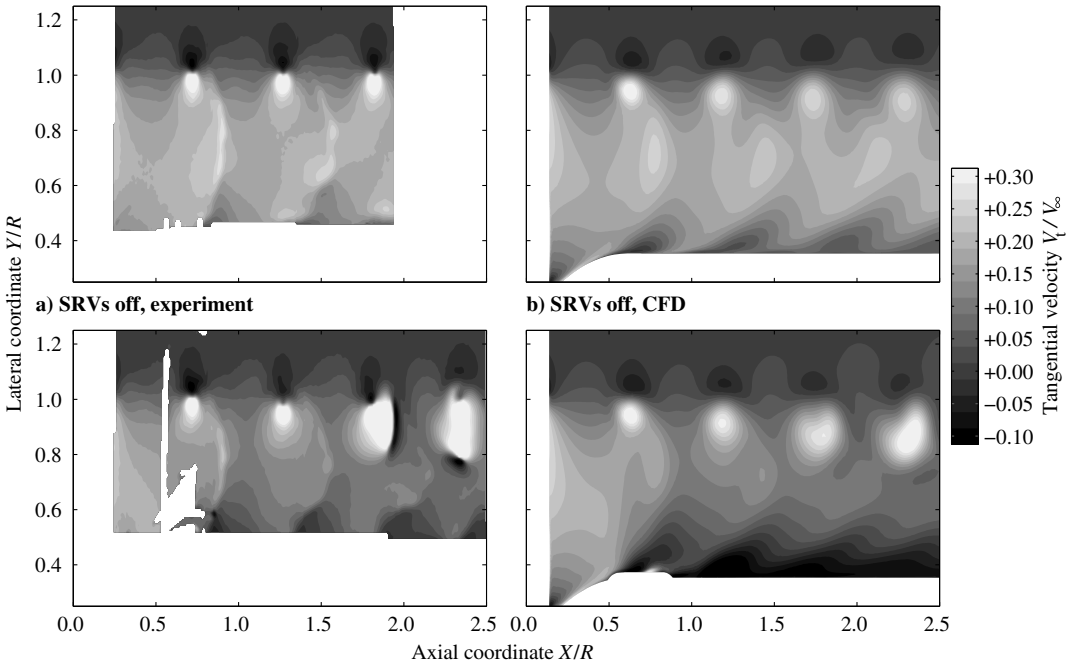

a) SRVs off, experiment **b) SRVs off, CFD**

c) SRVs on, experiment **d) SRVs on, CFD**

Fig. 9 Phase-locked tangential velocity in the propeller slipstream at $Z/R = 0.03$, $J = 1.40$.

the SRVs, a small increase in the tangential velocity occurred. This is due to the upwash induced by the loaded SRVs. The wakes of the propeller blades can be seen in the slipstream as vertical bands of increased tangential velocity (e.g., at $X/R = 0.9$), which become increasingly crescent when convecting downstream due to the nonuniform axial and tangential velocity distributions in the slipstream. The tip vortices of the propeller blades can be recognized by the pronounced velocity perturbations at the edge of the slipstream ($Y/R \approx 1.0$). At a streamwise coordinate of $X/R \approx 2.0$, the tip vortex from the nearest SRV entered the measurement plane at $Y/R \approx 0.9$ and started interacting with the tip vortex of the propeller blade. This is visualized in Fig. 10 by isosurfaces of the vorticity in axial direction extracted from the numerical simulations, confirming that the tip vortex of the SRV approaches the evaluation plane directly downstream of one of the tip vortices of the propeller blades. Moreover, it can be seen that the trajectory of the tip vortex from the SRV is affected by the passage of the tip vortices of the propeller blades, and as a result displays an oscillating behavior.

A qualitative agreement is obtained between the experimental and numerical data shown in Fig. 9. Compared to the PIV data, the CFD results suffer from numerical diffusion, smoothing the velocity gradients in the wakes and tip vortices of the propeller blades. As a result, these flow structures appear more spread out in the numerical

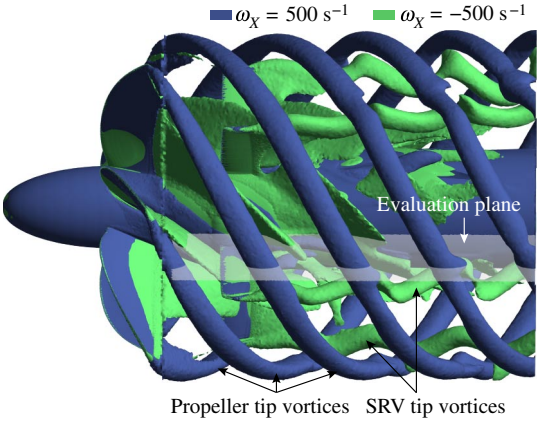

Fig. 10 Interaction between tip vortices of the SRVs and the propeller at $J = 1.40$.

data. This also applies to the tip vortex from the SRV, making its entrance into the measurement plane harder to discern in the CFD results than in the PIV data set. Apart from the effects due to numerical diffusion, also a phase shift can be observed between the

experimental and numerical results by comparing the axial locations of the blade tip vortices and wakes. To provide a quantitative comparison between the experimental and numerical data, profiles of the time-averaged tangential and axial velocity were extracted from the evaluation plane, at $X/R = 1.5$ downstream of the propeller. The corresponding results are given in Fig. 11, which include the data for all considered propeller thrust settings. For the experimental data, markers are plotted at every fifth data point for clarity. The uncertainty of the experimental data is indicated by the gray shading surrounding the measured average values.

The tangential-velocity profiles (Figs. 11a, 11c, and 11e) confirm the conclusions drawn from Fig. 9. The largest reductions in swirl were obtained in the radial part of the slipstream covered by the SRVs ($Y/R < 0.9$), whereas for $Y/R \geq 0.9$ no benefits could be achieved because of the cropping of the SRVs. Near the root of the SRVs, a negative tangential velocity occurred, indicating that the velocity induced by the SRVs overcompensated the original swirl in the propeller slipstream. At the high-thrust setting ($J = 1.05$; Fig. 11a), a tip vortex of one of the SRVs crossed near the considered evaluation location ($X/R = 1.5$). This caused the negative gradient in the tangential velocity around $0.7 < Y/R < 0.8$. As expected, this gradient was better resolved in the experiment than in the simulations. A good quantitative agreement is obtained between the PIV measurements and the CFD evaluations for the intermediate and low propeller thrust settings (Figs. 11c and 11e) in the middle part of the slipstream ($0.5 < Y/R < 0.9$). At more outboard lateral coordinates, near the slipstream edge, the CFD results suffered from numerical diffusion, as discussed before in relation to Fig. 9.

From the axial-velocity profiles (Figs. 11b, 11d, and 11f), it is concluded that, for the high-thrust condition ($J = 1.05$; Fig. 11b), the installation of the SRVs decreased the axial velocity at the measurement location over most of the considered radial extent. At this operating point, relatively high tangential velocities occur in the slipstream (Fig. 11a), causing a large inflow angle to the SRVs. The CFD simulations showed that this resulted in leading-edge separation over a large part of the span of the SRVs, reducing the axial velocity in the downstream part of the slipstream. This is discussed in more detail in Sec. III.B.2. At the intermediate- and low-thrust settings, on the other hand, the installation of the SRVs increased the axial velocity in the part of the slipstream in which the swirl was recovered ($Y/R < 0.85$). Comparing the experimental and numerical data, differences are again observed near the edge of the slipstream due to

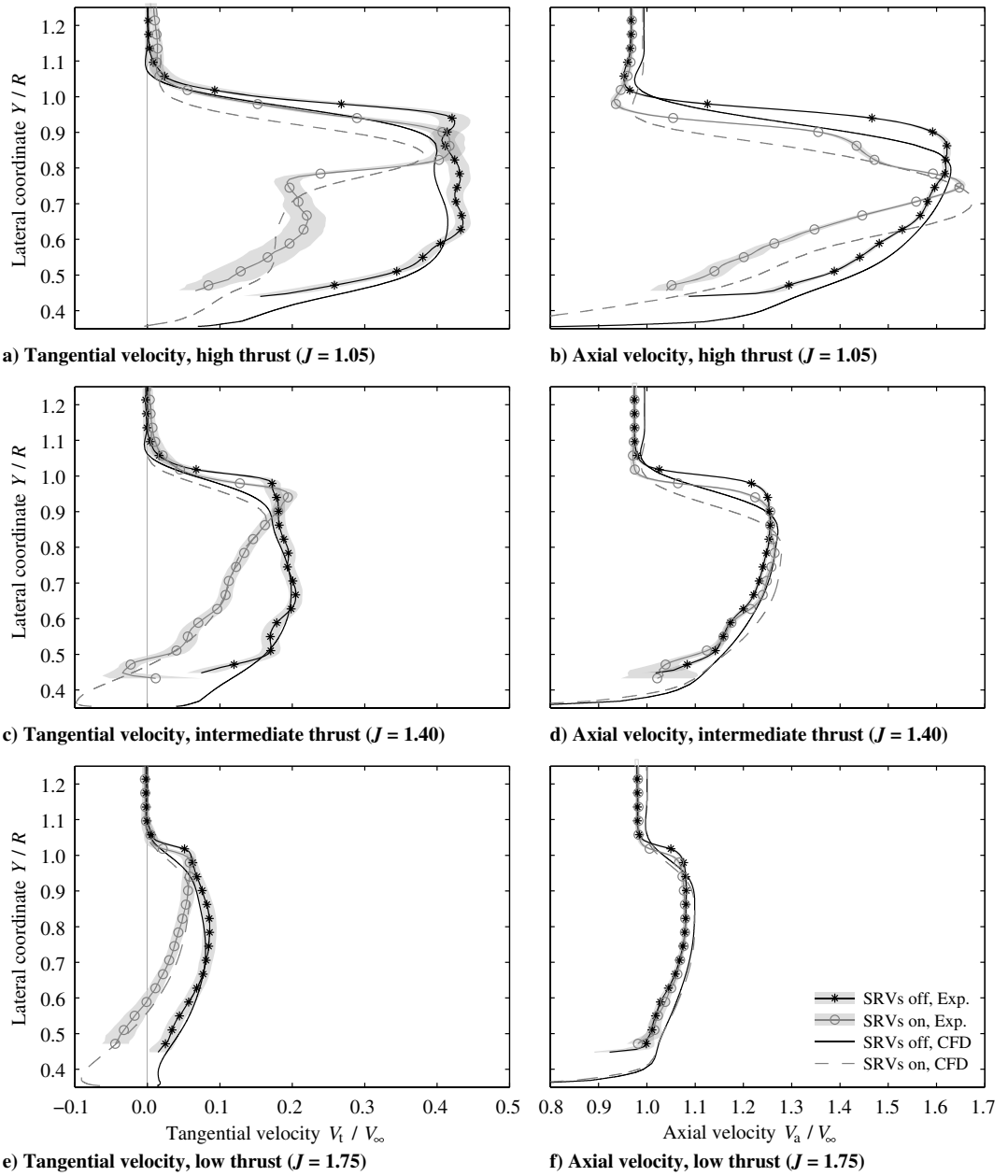

a) Tangential velocity, high thrust ($J = 1.05$) **b) Axial velocity, high thrust ($J = 1.05$)**

c) Tangential velocity, intermediate thrust ($J = 1.40$) **d) Axial velocity, intermediate thrust ($J = 1.40$)**

e) Tangential velocity, low thrust ($J = 1.75$) **f) Axial velocity, low thrust ($J = 1.75$)**

Fig. 11 Time-averaged velocity in the propeller slipstream at $X/R = 1.5$, $Z/R = 0.03$.

the smearing of the velocity gradients induced by the tip vortices of the propeller and the SRVs in the simulations. Away from the slipstream edge, the measured velocity is consistently lower than the simulated value. This offset occurs both for the configurations without and with the SRVs installed, and could point at an upstream effect of the support structure used in the experiment, which was not included in the simulations. However, considering the changes to the velocity distributions caused by the installation of the SRVs, it is observed that the simulations predict the same trends as measured in the experiment, at all thrust settings. Therefore, it is concluded that the numerical data can be used to assess the relative efficiency benefits achieved by the installation of the SRVs, which is the scope of Sec. III.B.

2. *Swirl Recovery*

The results shown in Figs. 9 and 11 are only representative of a single horizontal plane in the slipstream of the propeller–SRV configuration. To analyze the swirl recovery over the entire disk, Fig. 12 depicts the computed distribution of the tangential velocity in a plane perpendicular to the streamwise direction, again positioned at $X/R = 1.5$, for the intermediate-thrust setting ($J = 1.40$). The swirl recovery achieved by the installation of the SRVs occurred over the entire circumference of the slipstream, as expected. Because the SRVs are stationary, their wakes and tip vortices are clearly visible in the time-averaged flowfield (Fig. 12b) by the strong local modification of the tangential velocity.

To quantify the swirl-recovery performance of the SRVs, the changes in rotational and total kinetic-energy flow caused by the propulsion system were integrated over the disks shown in Fig. 12. Integration was performed up to a radial coordinate of $r/R = 1.3$, which was sufficiently far away from the slipstream edge to make sure all tangential velocity components had vanished to zero. Table 5 reports the ratio of rotational kinetic-energy flow to total kinetic-energy flow for the cases with and without the SRVs, at all considered propeller thrust settings. It can be seen that the relative contribution of the swirl component to the total kinetic-energy flow was decreased by the installation of the SRVs at all thrust settings. The swirl was reduced most effectively at the intermediate-thrust condition ($J = 1.40$), at which a reduction of 46% occurred compared to the isolated propeller.

B. Propulsive Performance

The propulsive efficiency of the propeller–SRV configuration depends on the thrust of both components and the propeller torque. The SRVs are designed to generate thrust by deflecting the flow in the propeller slipstream into the axial direction. In turn, the presence of the SRVs might affect the propeller performance due to upstream interference. Both effects are discussed separately.

Table 5 Change in ratio of rotational to total kinetic-energy flow due to installation of the SRVs

	$\Delta\dot{E}_{k_{rot}}/\Delta\dot{E}_{k_{tot}}$		
J	SRVs off, %	SRVs on, %	Change due to SRVs, %
1.05	8.46	5.50	−35
1.40	4.56	2.47	−46
1.75	2.02	1.32	−35

1. *Propeller Performance*

The presence of the downstream SRVs modifies the inflow experienced by the propeller, thereby possibly affecting the propeller performance. Before assessing the effects of the SRVs on the loading of the propeller, this subsection first characterizes the local blade loading for the isolated configuration without the SRVs installed. To validate the CFD results, the computed pressure distribution on the propeller blade at $r/R \approx 0.65$ was compared to the experimental result, as shown in Fig. 13a for the high-thrust condition ($J = 1.05$). The wide suction peak on the front part of the profile is due to a leading-edge vortex, which is visualized in Fig. 13b. This vortex is caused by the high sweep and thin leading edge of the propeller blade in combination with a large local angle of attack, and has been observed before in experiments on a propeller with a geometry comparable to the one considered in the current paper [28]. Near the trailing edge, a small suction region can be observed on the lower side of the blade. This is caused by the local curvature of the blade profile, which features a rounded trailing edge. The agreement between the experimental and numerical data is reasonably good, especially on the pressure side of the blade and around the suction region near the leading edge of the profile. The unexpected increase of the suction observed in the experimental data at $x/c = 0.7$ may have been caused by calibration shifts between the different pressure sensors instead of a physical phenomenon.

With the SRVs installed, the inflow to the propeller is modified when compared to the isolated propeller case. The axial component of the inflow velocity vector decreases due to blockage, whereas the local tangential velocity component experienced by the blade section decreases due to the upwash caused by the SRVs. Because these two effects oppose each other, the final modification of the propeller performance depends on the solidity of the SRVs, their loading, and the propeller–SRV spacing. Table 6 displays the measured and computed time-averaged propeller thrust and torque for the configurations with the SRVs on and off. The RSB only measured the forces and moments generated by the rotating part of the setup, so the contribution of the SRVs to the total propulsive performance is not included in Table 6. For consistency with the experimental results, the numerical data were obtained by integration of the pressure and shear stress acting on the propeller blades, hub, and spinner. A measure of

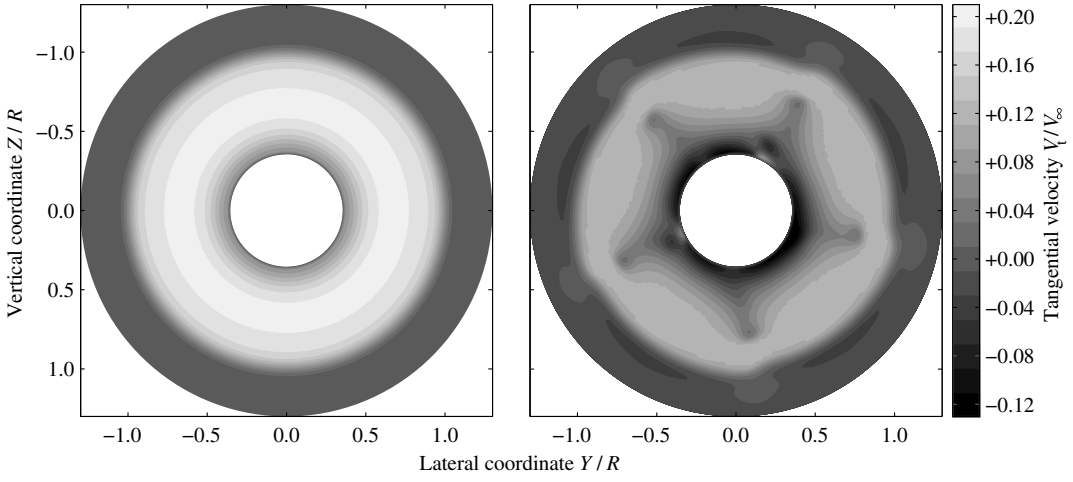

a) SRVs off **b) SRVs on**

Fig. 12 Computed time-averaged tangential velocity in the propeller slipstream at $X/R = 1.5$, $J = 1.40$.

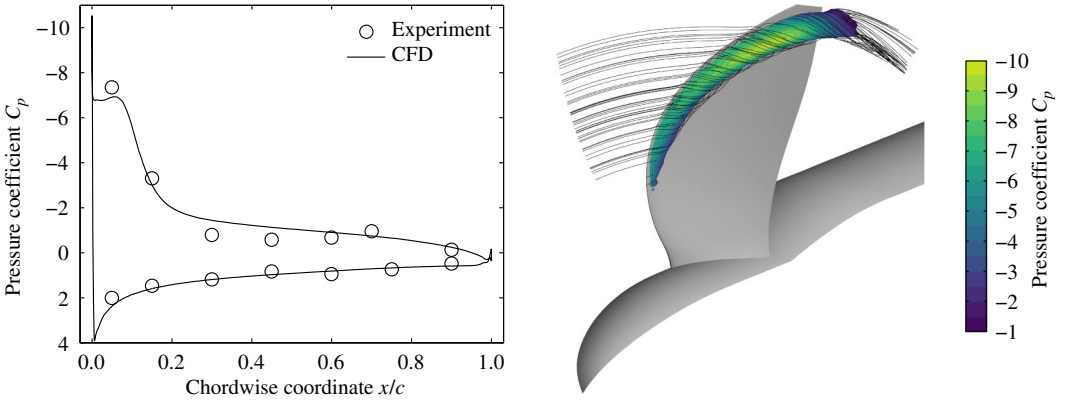

a) Pressure distribution at $r/R \approx 0.65$

b) Isosurface of turbulence kinetic energy at 1000 $m^2 \cdot s^{-2}$ with local streamlines

Fig. 13 Propeller-blade pressure distribution and visualization of leading-edge vortex at $J = 1.05$, SRVs off.

the variability of the experimental data was obtained by taking the standard deviation of repeated acquisitions for the isolated propeller.

The performance data provided in Table 6 show that the overall upstream effect of the SRVs on the time-averaged propeller performance was limited. The CFD analyses predicted a small but systematic increase in propeller thrust and torque of around 1% due to the installation of the SRVs at all operating conditions. In the experiment, the differences between the propeller thrust and torque obtained with and without the SRVs were within the variability of the RSB measurements. Therefore, no direct comparison can be made between the experimental and numerical data in terms of the effect of the SRVs on the propeller performance. The computed increase in loading with SRVs installed is in disagreement with previous experimental results published by Gazzaniga and Rose [5] and Dittmar and Hall [13], who showed an unloading of the propeller due to the installation of the SRVs. This is likely the result of differences in SRV solidity, loading, and propeller–SRV spacing, and not only affects the propulsive efficiency of the system, but also the acoustic performance, as discussed in Sec. III.C.

Comparing the absolute performance values from the experiment and the simulations, it can be seen that the torque coefficient computed in CFD is within 2% of the experimental data at all propeller operating points considered. For the thrust coefficient, on the other hand, this is only the case at $J = 1.05$ and $J = 1.40$. At the low-thrust condition ($J = 1.75$), the value predicted by CFD is approximately 10% lower than the measured value. It should be noted that the uncertainty of the RSB measurements was largest in this low-thrust condition, thereby possibly explaining part of the increased difference between the experimental and numerical results.

Whereas the change in time-averaged propeller performance due to the upstream effect of the SRVs was only around 1% of the performance of the isolated propeller, the flow perturbations induced by the SRVs might still have induced nonnegligible unsteady loading on the propeller blades. Figure 14 presents the unsteady component of the blade normal-force coefficient as a function of the circumferential position of the leading edge of the instrumented propeller blade. The circumferential positions of the SRVs (Fig. 2) are indicated by the dotted lines. For consistency with the experimental results, the unsteady normal force extracted from the CFD data was computed using the pressure forces only, neglecting the influence of the viscous forces. The measured unsteady blade-loading data displayed a dominant one-per-revolution sinusoidal perturbation due to a small flow angularity induced by the inflow measurement infrastructure. Because this effect was not related to the SRVs, it was removed from the data by subtracting the unsteady normal-force component measured for the isolated propeller. The error bars shown in Fig. 14 are indicative of the uncertainty of the experimental and numerical data. For the experimental data, the error bars represent the standard deviation of the measured unsteady normal-force coefficient, as computed from repeated measurements at constant operating conditions. For the numerical data, the error bars correspond to the standard deviation averaged over all blade positions, using the data available from the two blade passages from which the results were extracted.

Figure 14 confirms the expected perturbation of the propeller-blade loading due to the installation of the SRVs. A periodic loading cycle can be observed in both the experimental and numerical data, at a frequency equal to the number of SRV passages in one revolution. During an SRV passage, the sectional propeller-blade loading increased by a small but systematic amount at all propeller thrust settings. The peak-to-peak amplitude of the sectional normal-force coefficient equaled at most about 0.8% of the time-averaged result at the high-thrust setting ($J = 1.05$), increasing up to 2.3% at the lowest thrust setting ($J = 1.75$). The only significant differences between the experimental and numerical data occurred at the high-thrust condition ($J = 1.05$; Fig. 14a). The low-frequency sinusoidal perturbation on the measured signal in this condition is a remaining artifact related to the small inflow angularity in the experiment discussed previously, and hence should be ignored in comparison with the numerical data. However, the peak-to-peak amplitude of the measured unsteady loading is smaller than predicted by the simulations. This could be related to the finite frequency response of the pressure sensors, resulting in a smoothing of the peaks in the pressure response. However, it should be noted that the maximum

Table 6 Effect of SRVs on the time-averaged propeller performance

		C_T			C_Q		
J	Data	SRVs off	SRVs on	Difference, %	SRVs off	SRVs on	Difference, %
1.05	Experiment	0.509 ± 0.001	0.510 ± 0.001	N/A[a]	0.152 ± 0.001	0.152 ± 0.001	N/A[a]
	CFD	0.514	0.521	+1.4	0.155	0.157	+1.2
1.40	Experiment	0.356 ± 0.003	0.357 ± 0.003	N/A[a]	0.107 ± 0.001	0.106 ± 0.001	N/A[a]
	CFD	0.349	0.353	+1.1	0.109	0.110	+1.0
1.75	Experiment	0.184 ± 0.008	0.187 ± 0.008	N/A[a]	0.058 ± 0.003	0.055 ± 0.003	N/A[a]
	CFD	0.166	0.167	+1.0	0.059	0.059	+1.1

Difference defined as change due to installation of the SRVs.

[a]N/A = not applicable. Difference within repeatability of RSB measurements.

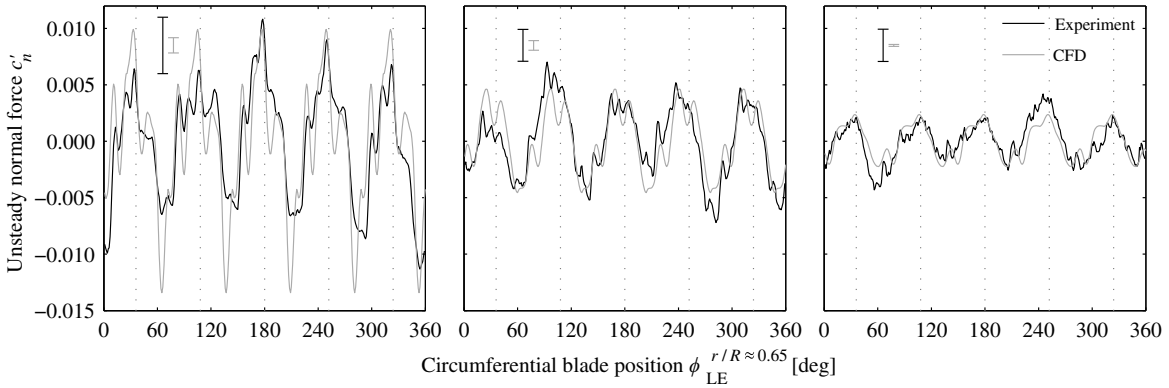

a) High thrust (J = 1.05) **b) Intermediate thrust (J = 1.40)** **c) Low thrust (J = 1.75)**

Fig. 14 Unsteady propeller-blade loading at $r/R \approx 0.65$ with SRVs on locations indicated by the dotted lines.

difference between the experiment and the simulation remains close to the uncertainty of the experimental data. At the intermediate- and low-thrust settings (Figs. 14b and 14c), a better agreement is observed between the experiment and the simulation: the unsteady loads are predicted correctly by the simulation both in terms of phase and amplitude.

2. *SRV Performance*

Because the SRVs used in the experiment were not instrumented, the CFD data were analyzed to extract the contribution of the SRVs to the system thrust. Table 7 presents the results in terms of the thrust generated by the SRVs and the associated increase in propulsive efficiency ($\Delta\eta = \eta_{\text{SRVs-on}} - \eta_{\text{SRVs-off}}$). Even though the SRVs are stationary, the thrust coefficient of the SRVs was defined based on the rotational speed and diameter of the propeller to allow for a direct comparison with the propeller's thrust contribution.

Table 7 shows that the SRVs generated a small amount of positive thrust at the high- and intermediate-thrust settings ($J = 1.05$ and $J = 1.40$), with a maximum associated efficiency gain of 0.7%. At the low-thrust condition ($J = 1.75$), on the other hand, the system thrust decreased due to the installation of the vanes. Although the SRVs generated a significant force in this condition, this force was not aligned with the thrust direction. As a result, despite of the swirl recovery achieved at the low-thrust setting (Table 5), the overall thrust of the propeller–SRV configuration decreased. The performance of the SRVs was investigated in more detail by considering the time-averaged radial distribution of the thrust at each of the studied advance ratios, as plotted in Fig. 15. The sectional thrust coefficient $c_{t_{\text{SRV}}}$ was computed by integration of the time-averaged pressure and shear-stress contributions acting on a radial segment of a single SRV.

The thrust distributions plotted in Fig. 15 indicate that the design of the SRVs could have been improved to maximize the propulsive performance. At the tip of the SRVs, where the pitch angle was decreased significantly (Fig. 3), a net drag force was generated at all propeller operating conditions considered. This signifies the importance of proper modeling of the flowfield near the edge of the propeller slipstream in the analysis code used during the design of the SRVs. Table 7 indicates that the SRVs performed best at the intermediate propeller thrust setting ($J = 1.40$). This is reflected in Fig. 15, which displays that a positive thrust force was generated at this operating point over a large part of the span ($0.54 < r/R_{\text{SRV}} < 0.97$). At the most inboard radial stations, on the other hand, a resultant drag force occurred due to flow separation. This is visualized in Fig. 16,

Table 7 Contribution of the SRVs to the propulsive performance

J	$C_{T_{\text{SRV}}}$	$\Delta\eta$
1.05	0.002	0.002
1.40	0.003	0.007
1.75	−0.002	−0.009

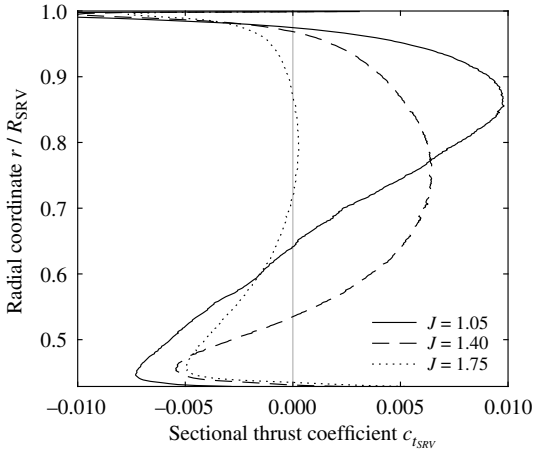

Fig. 15 Time-averaged radial distributions of the thrust on a single SRV.

which shows the shear lines on the SRV surface and the streamlines around a section near the root of the SRV, where the flow was clearly separated on the suction side of the vane. The local resultant drag force could have been prevented by a local increase of the pitch angle.

Figure 15 also indicates that it will be beneficial to change the SRV pitch angle as a function of the propeller loading condition. For the case at high propeller thrust ($J = 1.05$), for which the swirl is the largest (Fig. 11; Table 5), flow separation occurred on the SRVs over an even larger spanwise extent on the inboard part of the SRVs compared to the intermediate-thrust case, leading to a net drag force for $r/R_{\text{SRV}} < 0.65$. As a result, the propulsive performance of the SRVs was decreased at this operating point when compared to the intermediate-thrust setting ($J = 1.40$). This is in agreement with the results presented in Table 7, and could have been prevented by adopting a variable-pitch design of the SRVs [9]. At the lowest propeller thrust setting ($J = 1.75$), the SRVs generated drag over almost the entire span. In this condition, the swirl angle is relatively small, which reduces the potential for thrust generation by the SRVs.

Because the flowfield in the propeller slipstream is unsteady (Fig. 9), the SRVs experience an unsteady inflow with dominant perturbations caused by the propeller-blade wakes and tip vortices. This leads to cyclic loading around the time-averaged results displayed in Fig. 15. To compare the unsteady loads on the SRVs to those occurring on the propeller blades (Fig. 14), the time-accurate sectional normal force on the SRVs was extracted from the CFD data. Figure 17 presents the results with the time-averaged loading subtracted, at radial stations $r/R_{\text{SRV}} \approx 0.74$ and $r/R_{\text{SRV}} \approx 0.99$. The data obtained at $r/R_{\text{SRV}} \approx 0.74$ are representative of the unsteady loading on the SRVs caused by the impingement of the blade wake, whereas the results at $r/R_{\text{SRV}} \approx 0.99$ are dominated by the interaction with the blade tip vortex. Because the unsteady SRV loading is periodic at the blade-passage frequency (BPF), only a single blade passage (60 deg) is displayed. The shaded areas

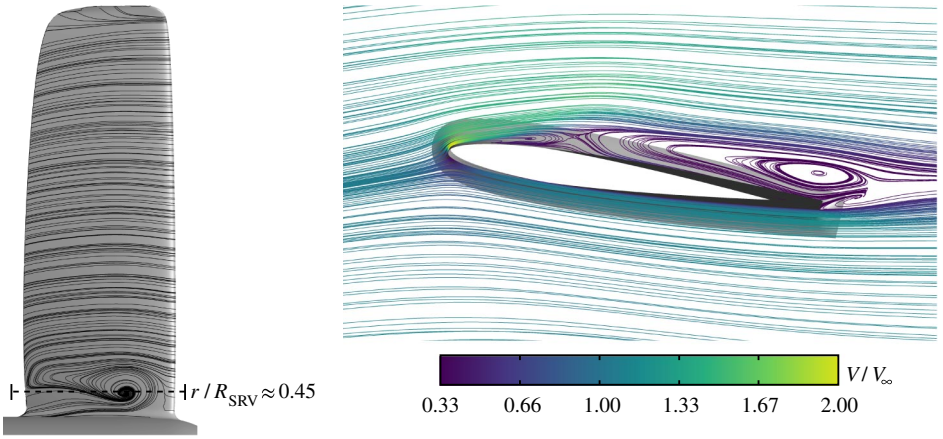

a) Shear lines on suction side **b) Streamlines at $r / R_{SRV} \approx 0.45$**

Fig. 16 Separation on the inboard part of the SRV at $J = 1.40$.

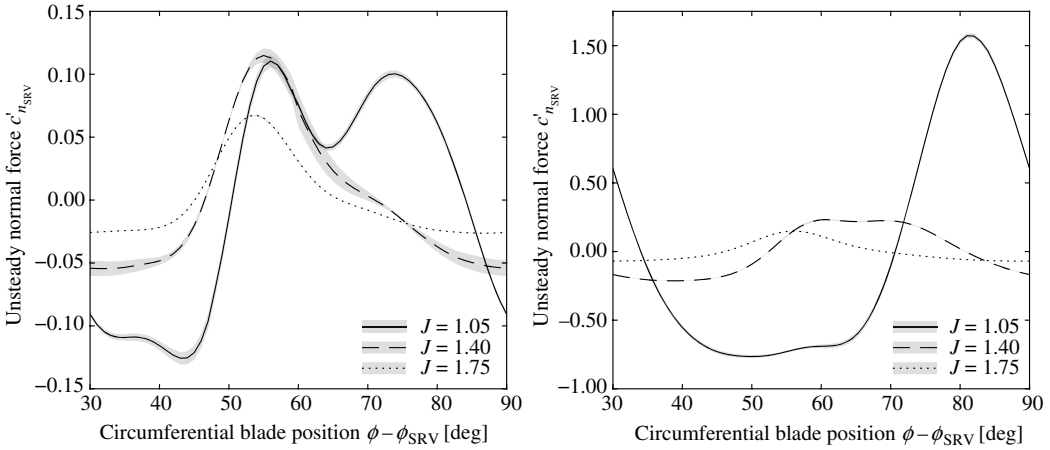

a) $r / R_{SRV} \approx 0.74$ ($r / R \approx 0.65$) **b) $r / R_{SRV} \approx 0.99$ ($r / R \approx 0.87$)**

Fig. 17 Unsteady SRV loading caused by propeller-slipstream impingement.

represent the standard deviation computed per blade position, using all data available from the two blade passages (120 deg) from which the numerical data were extracted. Note that the scales on the vertical axes of the two subplots are different.

The time histories of the unsteady normal-force coefficient on the SRVs at $r/R_{SRV} \approx 0.74$ (Fig. 17a) reveal a peak in the unsteady loading around $\phi - \phi_{SRV} = 55$ deg at all propeller thrust settings. At this position, the blade wake impinged on the downstream SRV, causing a sudden increase in local loading. The delay between the passage of the propeller blade in front of the SRV (at $\phi - \phi_{SRV} = 0$ deg) and the impingement of the blade wake on the SRV is caused by the finite distance between the propeller and the SRVs. This delay becomes larger with increasing propeller thrust setting due to the associated increase in the pitch angle of the slipstream helix. The pressure disturbance caused by the passing propeller blade itself might have amplified the unsteady loading due to the blade-wake impingement, but should not feature a phase shift with changing propeller thrust condition. Therefore, it can be considered as a secondary effect, dominated by the blade-wake impingement phenomenon.

At the highest thrust setting ($J = 1.05$), a secondary peak is observed in Fig. 17a at about 20 deg after the primary rise in the loading. This peak is attributed to the induced velocities caused by the propeller-blade tip vortex, which trails the blade wake (Fig. 9). The magnitude of this secondary peak in the unsteady SRV loading increases with increasing radial coordinate, as confirmed by Fig. 17b. Near the tip of the SRVs, the unsteady loading is about one order of magnitude larger than on the rest of the vane. At the low- and intermediate-thrust settings, the velocities induced by the tip vortex are smaller; hence, their effect on the unsteady SRV loading is also smaller.

The importance of the interaction between the SRVs and the propeller-blade tip vortices is highlighted in Fig. 18, which displays the spanwise distribution of the rms of the unsteady normal force on the SRVs for all considered propeller thrust settings. Especially at the high-thrust condition ($J = 1.05$), a clear peak in the unsteady loading occurs near the tip of the SRV. Upon decreasing the thrust setting, the strength of the propeller-blade tip vortices decreases, whereas the

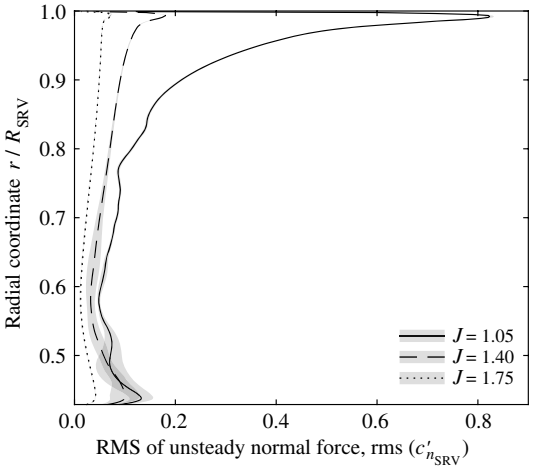

Fig. 18 Spanwise distribution of the unsteady SRV loading.

reduced slipstream contraction leads to a larger separation between the vortex cores and the SRVs. As a result, the unsteady loading decreases significantly compared to the case at high thrust, and the peak caused by the vortex interaction practically disappears.

Compared to the unsteady loading on the propeller blades (Fig. 14), the absolute amplitude of the load fluctuations on the SRVs was about one order of magnitude larger. This is in agreement with the results published by Li et al. [10] based on numerical simulations with a profile-transformation method. The absolute amplitude of the load oscillations increased with increasing propeller-blade loading (decreasing advance ratio), as expected. Relative to the time-averaged loading, on the other hand, the peak-to-peak amplitude of the unsteady loading amounted to approximately 20% at all thrust conditions considered (averaged over the span of the SRVs). Previous work for contrarotating propellers and turbomachinery has suggested that the unsteady loads on the SRVs may be decreased by increasing the propeller–SRV spacing [11], or using the active technique of blowing from the propeller [29,30].

C. Acoustic Performance

Although the installation of the SRVs increased the propulsive efficiency at the intermediate and high propeller thrust settings, it also introduced two additional noise sources. The upstream interaction of the SRVs with the propeller caused unsteady loading on the propeller blades (Fig. 14). Moreover, the time-dependent velocities induced by the propeller-blade wakes and tip vortices led to fluctuating loads on the SRVs (Figs. 17 and 18).

To investigate the noise penalty caused by the installation of the SRVs, both the tonal and broadband components of the sound emissions were considered. Figure 19 displays waveforms of the (phase-averaged) harmonic content of the noise emissions for the configurations with and without the SRVs, for all considered thrust settings. In addition, Fig. 20 provides sound spectra obtained at the high-thrust setting ($J = 1.05$), with the markers indicating the sound-pressure levels (SPLs) at frequencies corresponding to integer multiples of the propeller BPF. Furthermore, the spectrum of the background noise is included for reference. The sound spectra for the intermediate- and low-thrust settings are omitted because, for these cases, the broadband noise emissions of the propeller–SRV configuration were mostly below the background noise floor. Moreover, at $J = 1.75$, the fundamental tone could only be extracted from the recorded data using the phase-averaging technique, because its level was below that of the wind-tunnel noise. The data presented in Figs. 19 and 20 were acquired using the microphone positioned at an axial emission angle in the propeller plane ($\theta_e = 90$ deg) and a circumferential directivity angle of $\phi = 90$ deg.

Figures 19 and 20 highlight an increase in amplitude of the higher harmonics of the BPF with SRVs installed. For the isolated propeller, the sound emissions are dominated by the fundamental propeller tone at $1 \cdot BPF$. With the SRVs present, on the other hand, the noise emissions change significantly: additional high-frequency pressure oscillations are observed in the waveforms at all thrust settings (Fig. 19). At the high-thrust setting ($J = 1.05$), the amplitude of several of the higher harmonics increased by up to 16 dB due to the installation of the SRVs (Fig. 20).

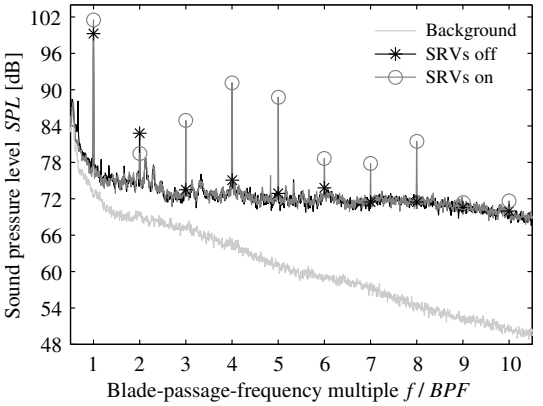

Fig. 20 Sound spectrum at $J = 1.05, \theta_e = 90$ deg, $\phi = 90$ deg.

The higher levels of the harmonics with SRVs installed impacted the overall tonal noise levels of the propeller–SRV configuration. This is best illustrated by the development of the cumulative tonal noise level ΣSPL with increasing number of harmonics included in the summation, defined as

$$\Sigma SPL = 20\log_{10}\frac{\mathrm{rms}\left(\sum_{i=1}^{n_{\mathrm{BPF}}} p_{i\cdot\mathrm{BPF}}\right)}{20 \cdot 10^{-6}} \tag{1}$$

in which n_{BPF} is the number of BPF multiples included in the summation, and $p_{i\cdot\mathrm{BPF}}$ is the acoustic pressure associated with the tone at the ith multiple of the BPF. Equation (1) was evaluated for the first 10 multiples of the BPF, considering the configurations with and without the SRVs installed. The results are plotted in Fig. 21. For the isolated propeller, the level of the fundamental tone was practically equal to the total tonal noise level based on a summation of the first 10 tones, for all propeller thrust settings. With the SRVs installed, the cumulative tonal noise level increased significantly upon including additional harmonics. The importance of the high-frequency content to the tonal SPL was found to increase with increasing advance ratio due to the associated reduction of the time-averaged propeller-blade loading. Note that at the intermediate- and low-thrust settings, the cumulative tonal noise level based on the first propeller tones was lower with SRVs installed than for the isolated propeller. This was due to destructive interference between the noise sources associated with the isolated propeller and the SRVs. This also explains the reduction in strength of the tone at $2 \cdot BPF$ for the case at $J = 1.05$ (Fig. 20).

The increase in the tonal noise emissions with SRVs installed is in disagreement with the results published by Dittmar and Hall [13]. However, in their case, the measured decrease of the noise emissions was attributed to the observed unloading of the propeller with the SRVs installed, which did not occur in the current study, as discussed in relation to Table 6. In contrast to the tonal noise emissions,

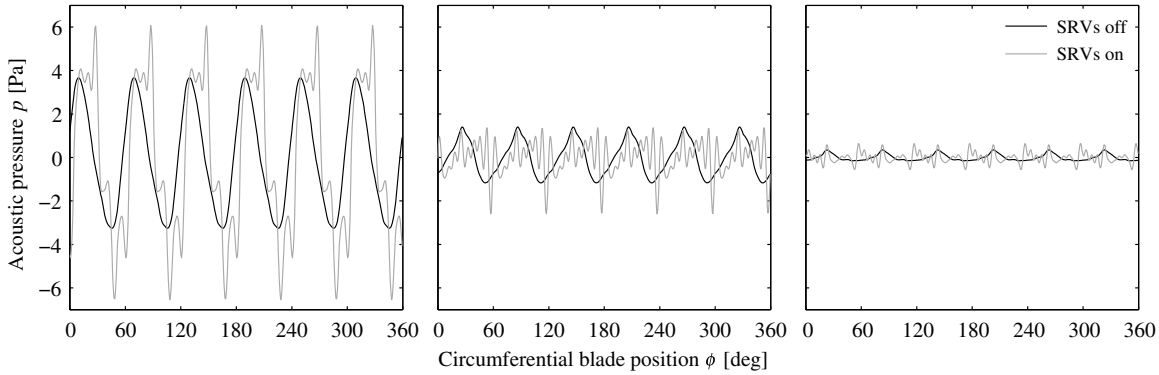

a) High thrust (J = 1.05) **b) Intermediate thrust (J = 1.40)** **c) Low thrust (J = 1.75)**

Fig. 19 Acoustic-pressure waveforms at $\theta_e = 90$ deg, $\phi = 90$ deg.

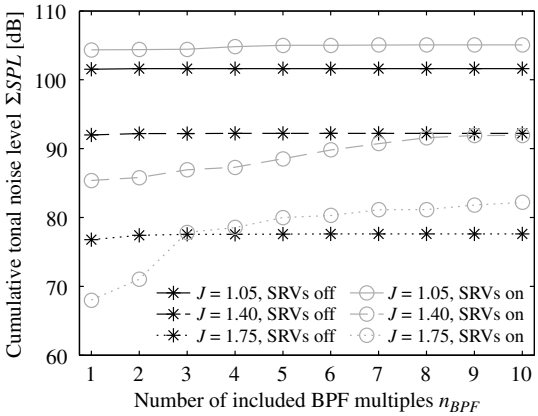

Fig. 21 Cumulative tonal SPL with increasing number of included harmonics at $\theta_e = 90$ deg, $\phi = 90$ deg.

the broadband component was not affected by the installation of the SRVs at the high-thrust setting (Fig. 20). Therefore, it is concluded that for this propeller operating point, the broadband noise generated by the isolated propeller dominated the broadband noise emitted from the SRVs. For the intermediate- and low-thrust settings, the broadband emissions from the propeller–SRV configuration were too low to be distinguished from the background noise, and hence no conclusions can be drawn regarding the impact of the installation of the SRVs on the broadband noise levels for these propeller settings.

To study the directivity of the noise emissions with the SRVs installed, the microphone measurements were taken over a range of axial directivity angles θ (defined in Fig. 5). Figure 22 presents the resulting summed tonal noise levels (based on the first 10 tones) as a function of the axial emission angle. The SPLs were scaled to a constant observer distance, equal to the distance between the propeller center and the microphone corresponding to $\theta_e = 90$ deg ($r_{mic} = 2.84$ m). The directivity patterns recorded for the isolated propeller feature a number of unexpected irregularities. This was due to interference between the various noise sources, which was confirmed by analysis of the waveforms of the acoustic pressure.

Figure 22 shows that the impact of the installation of the SRVs on the tonal noise emissions varies with the propeller thrust setting. Integrated over the considered axial emission range, noise penalties of 3, 5, and 7 dB were measured for the high-, intermediate-, and low-thrust conditions, respectively. At the high-thrust setting ($J = 1.05$; Fig. 22a), the noise sources associated with the isolated propeller were dominant in the forward direction ($\theta_e < 90$ deg). Because the steady-loading noise source decreases in amplitude with decreasing propeller thrust setting, the additional noise caused by the installation of the SRVs became significant over the entire directivity range at the lowest thrust setting ($J = 1.75$; Fig. 22c). In this condition, the noise penalty was mainly due to an increase in the SPLs of the higher harmonics (Fig. 21).

IV. Conclusions

This paper has discussed the aerodynamic and aeroacoustic performance of a propeller combined with swirl-recovery vanes (SRVs), targeted at enhancing the propulsive efficiency of single-rotating propellers. The SRVs convert the swirl in the propeller slipstream into thrust, thereby lowering the thrust requirement for the propeller. In this way, the required power input to the propeller can be reduced, and hence the efficiency of the propulsion system can be increased.

Based on both experimental and numerical methods, it was shown that the tested SRVs decreased the relative time-averaged tangential velocity in the propeller slipstream. At an intermediate-thrust condition, the simulations predicted a reduction in relative rotational kinetic energy of approximately 46% due to the application of the SRVs. Consequently, the propulsive efficiency increased by 0.7% at this operating condition. The performance of the SRVs was limited by stall occurring on the inboard part of the vane, which could have been prevented by a local increase of the pitch angle. Furthermore, it was concluded that a variable-pitch design would help to maintain the efficiency increase over a wide range of propeller loading conditions.

The installation of the SRVs introduces two aerodynamic interaction mechanisms. The upstream perturbation of the flowfield experienced by the propeller leads to fluctuating propeller loads. The peak-to-peak amplitude of the blade normal force at $r/R \approx 0.65$ was 1–2% of the local time-averaged loading, with the highest relative unsteady loads occurring at the lowest propeller thrust setting. The integrated propeller loading, on the other hand, remained practically unaffected, with a maximum increase in thrust and torque of 1% compared to the case of the isolated propeller. In addition to the upstream interaction, the downstream impingement of the propeller-blade wakes and tip vortices on the SRVs causes unsteady SRV loading. The amplitude of the unsteady loads increases toward the tip of the SRV due to the strong interaction with the propeller-blade tip vortices. Averaged over the span, the peak-to-peak amplitude of the unsteady SRV loading was equal to approximately 20% of the time-averaged result.

The unsteady interactions between the propeller and the SRVs introduce two additional noise sources. Far-field microphone measurements showed that the installation of the SRVs increased the tonal noise emissions, whereas the recorded broadband noise emissions were not affected. The increase in tonal noise was manifested mostly by a significant amplification of the levels of the higher harmonics. This especially affected the system noise emissions at low propeller thrust settings, for which the noise penalty was up to 7 dB. At higher thrust settings, more representative of flight, the tonal noise penalty was lower at 3–5 dB.

The current study has shown that SRVs can successfully be applied to enhance the propulsive efficiency of single-rotating propeller configurations. However, this came at the cost of a clear noise penalty compared to the isolated propeller setup. A multidisciplinary optimization of the SRV design could be employed to minimize the interaction-noise penalty while maximizing the aerodynamic benefits.

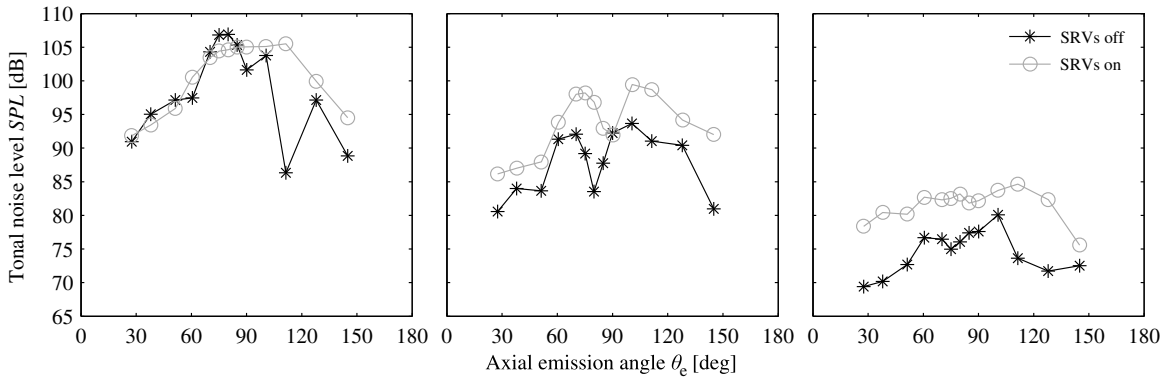

a) High thrust ($J = 1.05$) b) Intermediate thrust ($J = 1.40$) c) Low thrust ($J = 1.75$)

Fig. 22 Axial directivity of tonal noise levels at $\phi = 90$ deg.

Acknowledgments

The experimental results presented in this paper were obtained by the APIAN In Nonuniform Flow (APIAN-INF) research partners in the framework of the transnational access program organized by the European Strategic Wind Tunnels Improved Research Potential (ESWIRP) consortium, as part of the ESWIRP project. The research leading to these results has received funding from the European Union Seventh Framework Programme (FP7-INFRASTRUCTURE-2008-1) under the grant agreement number 227816. The authors would like to thank Hermann Holthusen for his efforts in the preparation and execution of the test campaign, and his input during the analysis of the data. Furthermore, the contributions of Kyle P. Lynch to the preparation, acquisition, and processing of the particle-image-velocimetry measurements are much appreciated. Finally, special thanks go to Jesse van Kuijk for defining the design of the swirl-recovery vanes.

References

[1] Guynn, M. D., Berton, J. J., Haller, W. J., Hendricks, E. S., and Tong, M. T., "Performance and Environmental Assessment of an Advanced Aircraft with Open Rotor Propulsion," NASA TM-2012-217772, Oct. 2012.

[2] Hoff, G. E., "Experimental Performance and Acoustic Investigation of Modern, Counterrotating Blade Concepts," NASA CR-185158, Jan. 1990.

[3] Negulescu, C., "Airbus AI-PX7 CROR Design Features and Aerodynamics," *SAE International Journal of Aerospace*, Vol. 6, No. 2, 2013, pp. 626–642. doi:10.4271/2013-01-2245

[4] Stürmer, A., Marquez Gutierrez, C. O., Roosenboom, E. W. M., Schröder, A., Geisler, R., Pallek, D., Agocs, J., and Neitzke, K.-P., "Experimental and Numerical Investigation of a Contra Rotating Open-Rotor Flowfield," *Journal of Aircraft*, Vol. 49, No. 6, 2012, pp. 1868–1877. doi:10.2514/1.C031698

[5] Gazzaniga, J. A., and Rose, G. E., "Wind Tunnel Performance Results of Swirl Recovery Vanes as Tested with an Advanced High Speed Propeller," *28th Joint Propulsion Conference and Exhibit*, AIAA Paper 1992-3770, July 1992. doi:10.2514/6.1992-3770

[6] Yamamoto, O., "Numerical Calculation of Propfan/Swirl Recovery Vane Flow Field," *28th Joint Propulsion Conference and Exhibit*, AIAA Paper 1992-3771, July 1992. doi:10.2514/6.1992-3771

[7] Wang, Y., Li, Q., Eitelberg, G., Veldhuis, L. L. M., and Kotsonis, M., "Design and Numerical Investigation of Swirl Recovery Vanes for the Fokker 29 Propeller," *Chinese Journal of Aeronautics*, Vol. 27, No. 5, 2014, pp. 1128–1136. doi:10.1016/j.cja.2014.03.009

[8] Li, Q., Öztürk, K., Sinnige, T., Ragni, D., Wang, Y., Eitelberg, G., and Veldhuis, L. L. M., "Design and Experimental Validation of Swirl Recovery Vanes for Propeller Propulsion Systems," *35th AIAA Applied Aerodynamics Conference*, AIAA Paper 2017-3571, June 2017. doi:10.2514/6.2017-3571

[9] Stokkermans, T. C. A., van Arnhem, N., and Veldhuis, L. L. M., "Mitigation of Propeller Kinetic Energy Losses with Boundary Layer Ingestion and Swirl Recovery Vanes," *Proceedings of the 2016 Applied Aerodynamics Research Conference*, Royal Aeronautical Soc., London, 2016, pp. 56–69.

[10] Li, Q., Wang, Y., and Eitelberg, G., "An Investigation of Tip Vortices Unsteady Interaction for Fokker 29 Propeller with Swirl Recovery Vane," *Chinese Journal of Aeronautics*, Vol. 29, No. 1, 2016, pp. 117–128. doi:10.1016/j.cja.2015.12.004

[11] Dring, R. P., Joslyn, H. D., Hardin, L. W., and Wagner, J. H., "Turbine Rotor-Stator Interaction," *Journal of Engineering for Power*, Vol. 104, No. 4, 1982, pp. 729–742. doi:10.1115/1.3227339

[12] Rai, M. M., "Navier-Stokes Simulations of Rotor/Stator Interaction Using Patched and Overlaid Grids," *Journal of Propulsion and Power*, Vol. 3, No. 5, 1987, pp. 387–396. doi:10.2514/3.23003

[13] Dittmar, J. H., and Hall, D. G., "Cruise Noise of an Advanced Propeller with Swirl Recovery Vanes," *Journal of Aircraft*, Vol. 30, No. 2, 1993, pp. 221–226. doi:10.2514/3.56885

[14] Frota, J., and Maury, E., "Analysis of APIAN High Speed Isolated Test Results—Acoustics and Aerodynamics," *Air & Space Europe*, Vol. 3, Nos. 3–4, 2001, pp. 87–92. doi:10.1016/S1290-0958(01)90064-4

[15] Drela, M., and Youngren, M. H., "XROTOR Download Page," 2011, http://web.mit.edu/drela/Public/web/xrotor/ [retrieved 28 Nov. 2013].

[16] Wieneke, B., "PIV Uncertainty Quantification from Correlation Statistics," *Measurement Science and Technology*, Vol. 26, No. 7, 2015, Paper 074002. doi:10.1088/0957-0233/26/7/074002

[17] Welch, P. D., "The Use of Fast Fourier Transform for the Estimation of Power Spectra: A Method Based on Time Averaging over Short, Modified Periodograms," *IEEE Transactions on Audio and Electroacoustics*, Vol. 15, No. 2, 1967, pp. 70–73. doi:10.1109/TAU.1967.1161901

[18] Anon., "Help System ANSYS® Academic Research Release 16.0, CFX," Software, 2015.

[19] Roosenboom, E. W. M., and Schröder, A., "Flowfield Investigation at Propeller Thrust Reverse," *Journal of Fluids Engineering*, Vol. 132, No. 6, 2010, Paper 061101. doi:10.1115/1.4001677

[20] Ortun, B., Boisard, R., and Gonzalez-Martino, I., "In-Plane Airloads of a Propeller with Inflow Angle: Prediction vs. Experiment," *30th AIAA Applied Aerodynamics Conference*, AIAA Paper 2012-2778, June 2012. doi:10.2514/6.2012-2778

[21] Barth, T. J., and Jespersen, D. C., "The Design and Application of Upwind Schemes on Unstructured Meshes," *27th Aerospace Sciences Meeting*, AIAA Paper 1989-366, Jan. 1989. doi:10.2514/6.1989-366

[22] Spalart, P. R., and Rumsey, C. L., "Effective Inflow Conditions for Turbulence Models in Aerodynamic Calculations," *AIAA Journal*, Vol. 45, No. 10, 2007, pp. 2544–2553. doi:10.2514/1.29373

[23] Roache, P. J., "Quantification of Uncertainty in Computational Fluid Dynamics," *Annual Review of Fluid Mechanics*, Vol. 29, No. 1, 1997, pp. 123–160. doi:10.1146/annurev.fluid.29.1.123

[24] Nallasamy, N., Yamamoto, O., Warsi, S., and Bober, L. J., "Large-Scale Advanced Propeller Blade Pressure Distributions—Prediction and Data," *Journal of Propulsion and Power*, Vol. 7, No. 3, 1991, pp. 452–461. doi:10.2514/3.23347

[25] Ekaterinaris, J. A., "High-Order Accurate, Low Numerical Diffusion Methods for Aerodynamics," *Progress in Aerospace Sciences*, Vol. 41, Nos. 3–4, 2005, pp. 192–300. doi:10.1016/j.paerosci.2005.03.003

[26] Eça, L., and Hoekstra, M., "Discretization Uncertainty Estimation Based on a Least Squares Version of the Grid Convergence Index," *2nd Workshop on CFD Uncertainty Analysis*, Instituto Superior Técnico, Oct. 2006.

[27] Sinnige, T., Ragni, D., Malgoezar, A. M. N., Eitelberg, G., and Veldhuis, L. L. M., "APIAN-INF: An Aerodynamic and Aeroacoustic Investigation of Pylon-Interaction Effects for Pusher Propellers," *CEAS Aeronautical Journal*, Vol. 9, No. 2, 2018, pp. 291–306. doi:10.1007/s13272-017-0247-2

[28] Klein, C., Henne, U., Sachs, W. E., Hock, S., Falk, N., Ondrus, V., Beifuss, U., and Schaber, S., "Pressure Measurement on Rotating Propeller Blades by Means of the Pressure-Sensitive Paint Lifetime Method," *New Results in Numerical and Experimental Fluid Mechanics IX*, edited by A. Dillmann, G. Heller, E. Krämer, H.-P. Kreplin, W. Nitsche, and U. Rist, Vol. 124, Notes on Numerical Fluid Mechanics and Multidisciplinary Design, Springer International Publishing, Cham, Switzerland, 2014, pp. 535–544. doi:10.1007/978-3-319-03158-3_54

[29] Akkermans, R. A. D., Stürmer, A., and Delfs, J. W., "Active Flow Control for Interaction Noise Reduction of Contra-Rotating Open Rotors," *AIAA Journal*, Vol. 54, No. 4, 2016, pp. 1413–1423. doi:10.2514/1.J053756

[30] Wo, A. M., Lo, A. C., and Chang, W. C., "Flow Control via Rotor Trailing Edge Blowing in Rotor/Stator Axial Compressor," *Journal of Propulsion and Power*, Vol. 18, No. 1, 2002, pp. 93–99. doi:10.2514/2.5902

C. S. Tan
Associate Editor